Magnetic Resonance Materials in Physics, Biology and Medicine (2019) 32:461–471
https://doi.org/10.1007/s10334-019-00742-6

RESEARCH ARTICLE

Detection of axonal degeneration in a mouse model of Huntington's disease: comparison between diffusion tensor imaging and anomalous diffusion metrics

Rodolfo G. Gatto[1,2] · Allen Q. Ye[2] · Luis Colon-Perez[3,4] · Thomas H. Mareci[4] · Anna Lysakowski[1] · Steven D. Price[1] · Scott T. Brady[1] · Muge Karaman[2,5] · Gerardo Morfini[1] · Richard L. Magin[2]

Received: 28 September 2018 / Revised: 31 December 2018 / Accepted: 29 January 2019 / Published online: 15 February 2019

Abstract

Objective The goal of this work is to study the changes in white matter integrity in R6/2, a well-established animal model of Huntington's disease (HD) that are captured by ex vivo diffusion imaging (DTI) using a high field MRI (17.6 T).

Materials and methods DTI and continuous time random walk (CTRW) models were used to fit changes in the diffusion-weighted signal intensity in the corpus callosum of controls and in R6/2 mice.

Results A significant 13% decrease in fractional anisotropy, a 7% increase in axial diffusion, and a 33% increase in radial diffusion were observed between R6/2 and control mice. No change was observed in the CTRW beta parameter, but a significant decrease in the alpha parameter (− 21%) was measured. Histological analysis of the corpus callosum showed a decrease in axonal organization, myelin alterations, and astrogliosis. Electron microscopy studies demonstrated ultrastructural changes in degenerating axons, such as an increase in tortuosity in the R6/2 mice.

Conclusions DTI and CTRW diffusion models display quantitative changes associated with the microstructural alterations observed in the corpus callosum of the R6/2 mice. The observed increase in the diffusivity and decrease in the alpha CTRW parameter providing support for the use of these diffusion models for non-invasive detection of white matter alterations in HD.

Keywords Magnetic resonance imaging · Diffusion tensor imaging · Anomalous diffusion · Huntington disease · Mice

Introduction

Huntington's disease (HD) is a fatal, inherited neurodegenerative disorder affecting over 30,000 people in the United States alone, with no effective therapeutic strategies available to cure or slow disease progression at present [1, 2]. Major HD clinical symptoms include movement abnormalities and cognitive deficits, which result from mutations in the Huntingtin gene (HTT), which causes expansion of a polyglutamine region in the encoded mutant huntingtin protein (mHTT) [3, 4]. mHTT is toxic to medium spiny neurons in the striatum and cortical pyramidal neurons in patients affected with HD [4, 5]. The disease affects the whole brain with the most damage occurring in the basal ganglia, which plays a key role in coordinating movement and behavior. Although there is no cure for HD, advances in diagnosis and the management of symptoms rely on the availability of animal models.

Several rodent models display the principal HD symptoms, and they are the focus of research investigations into

Rodolfo G. Gatto and Allen Q. Ye contributed equally to this work.

Electronic supplementary material The online version of this article (https://doi.org/10.1007/s10334-019-00742-6) contains supplementary material, which is available to authorized users.

✉ Richard L. Magin
rmagin@uic.edu

1 Department of Anatomy and Cell Biology, University of Illinois at Chicago, Chicago, IL, USA

2 Department of Bioengineering, University of Illinois at Chicago, 851 S Morgan St, 218 SEO (MC 063), Chicago, IL 60607, USA

3 Department of Neurology and Behavior, University of California at Irvine, Irvine, CA, USA

4 Department of Biochemistry and Molecular Biology, University of Florida, Gainesville, FL, USA

5 Center for MR Research, University of Illinois at Chicago, Chicago, IL, USA

the pathogenic mechanisms of HD [6]. Among the various rodent models available [6], the R6/2 mouse—expressing mHTT from the human HTT gene—is the most widely used [7]. The R6/2 mouse displays an early onset of the cognitive, behavioral, and locomotor HD symptoms (day 80) in the absence of overt cell death [8, 9]. Accordingly, pathological and experimental data established HD as a dying back neuropathy, where synaptic dysfunction and axonal degeneration represent early pathogenic events [4]. Direct evidence supporting this notion was obtained using YFP-R6/2 reporter mice, which feature fluorescently labeled HD-vulnerable cortical projection neurons in the corpus callosum [10]. In addition, in this work, diffusion tensor imaging (DTI) revealed a reduction in the fractional anisotropy (FA) in the corpus callosum of R6/2 mice (P30 days) before the onset of motor symptoms, an observation consistent with results from magnetic resonance imaging (MRI) studies in presymptomatic HD patients [11–14]. Collectively, these findings highlight the need for additional brain imaging procedures that follow axonal degeneration in HD throughout the entire time course of the disease.

A number of diffusion-weighted imaging approaches (intra-voxel incoherent motion [15], kurtosis imaging [16], and multi-shell DTI models [17]) have been used to evaluate the sub-voxel structure of the microporous white and gray matter of the brain. However, with the exception of kurtosis imaging, these techniques use low-to-medium amounts of diffusion-weighting (b values, typically less than 1000 s/mm^2) that investigate Gaussian or normal diffusion. Recently, higher ranges of b values have been used to examine non-Gaussian, so-called, anomalous diffusion (AD) models. Here, we will focus on the continuous time random walk (CTRW) model of diffusion that extends conventional Brownian motion by allowing the water molecule to be trapped (sub-diffusion) or released (super-diffusion), as it explores its local environment [18]. The CTRW model encodes this exploration in terms of the diffusion parameters (α, β, $D_{\alpha,\beta}$), which have been shown to exhibit contrast in diffusion studies of normal [18, 19] and diseased [20–22] brain tissue, e.g., they revealed sub-voxel changes in the brain [23–25].

The CTRW model complements the standard DTI model in two ways. First, while DTI describes diffusion anisotropy by applying gradients in many directions at b values less than 1000 mm^2/s, CTRW focuses on compartmental complexity in a few gradient directions with b values typically greater than 2000 mm^2/s. DTI is excellent at describing orthotropic tissues such as brain white matter and skeletal muscle, in situations, where the diffusion is generally Gaussian; CTRW is sensitive to sub-voxel structure through a statistical assignment of particle waiting times and jump displacements that generalize normal Brownian motion to anomalous diffusion. Biological tissue heterogeneity leads to restricted diffusion at intermediate length scales (micron-to-millimeter lengths), where intra- and extra-cellular structures trap water in organelles, between membranes, and throughout the network of fibers that organize cell molecular traffic. Local tissue perfusion in and around capillaries and active transport within axons is captured in the CTRW model by the assignment of rare, but large particle displacements.

In this study, we investigate the sensitivity of the CTRW parameters as biomarkers for HD and use optical microscopy to identify the structural basis of the underlying tissue changes. We first describe how we acquired ultra-high field (17.6 T) diffusion-weighted images of fixed mouse brains (ex vivo) from control (wild-type mice) and diseased (symptomatic R6/2 HD mice) animals. Then, we outline how the multi-directional, multiple b value images were analyzed using the standard DTI diffusion model (diffusivity and fractional anisotropy) and an anomalous diffusion non-Gaussian model (fractional-order and diffusion biomarkers). We next present results comparing DTI and anomalous diffusion models in regions of the corpus callosum known to be affected at the early stages of HD in R6/2 mice. Specifically, we found changes in FA and the fractional-order α parameter that were correlated with microstructural changes observed using light and electron microscopy. The paper ends with a discussion of the potential impact of these results on the early diagnosis of axonal pathology in HD, and the conclusion that the anomalous diffusion model should be included in future clinical studies.

Theory (anomalous diffusion)

The model of anomalous diffusion used in this paper is based on the CTRW extension of Brownian motion [26, 27]. Mathematically, the model is implemented by generalizing both the space and the time derivatives in Fick's first and second laws of diffusion to non-integer powers using fractional calculus [28]. Statistically, this approach considers particle motion characterized by separate inverse power law distributions of jump lengths and waiting times: a non-Gaussian stochastic process that captures the complex microenvironment in brain tissue [29–32]. The resulting diffusion propagator, $P(x,t)$, in one dimension is the solution to the following fractional-order partial differential equation version of Fick's second law:

$$\frac{\partial^{\alpha} P(x,t)}{\partial t^{\alpha}} = D_{\alpha,\beta} \frac{\partial^{\beta} P(x,t)}{\partial |x|^{\beta}}. \tag{1}$$

The operator on the left-hand side of Eq. (1) represents the Caputo fractional derivative in time for $0 < \alpha \leq 1$, and the operator on the right represents the symmetric Riesz fractional derivative in space for $1 < \beta \leq 2$, where $D_{\alpha,\beta}$ (mm$^{\beta}$/s$^{\alpha}$) is the fractional-order diffusion coefficient [33]. In the

case of $\alpha = 1$ and $\beta = 2$, Eq. (1) reverts to the classical integer order form of Fick's second law of diffusion [15]. For a point source at the origin of an unbounded medium, the solution to Eq. (1) can be obtained using the Laplace and Fourier transforms [34], which in the Fourier domain of spatial frequencies (k), gives

$$p(k,t) = E_{\alpha}(-D_{\alpha,\beta}|k|^{\beta}t^{\alpha}). \quad (2)$$

In Eq. (2), $E_{\alpha}(z) = \sum_{n=0}^{\infty} z^n / \Gamma(\alpha n + 1)$, is the Mittag–Leffler function and $\Gamma(\alpha n + 1)$ is the Gamma function [18]. The Mittag–Leffler function interpolates between the stretched exponential and power law decay over its domain [0, ∞] and converges to the exponential when $\alpha = 1$ and $\beta = 2$ [35]. Under the restriction of short diffusion, gradient pulses, $p(k,t)$, can be estimated in a diffusion-weighted MRI experiment [27].

Materials and methods

Animals

Experiments were performed under protocols approved by the Animal Care Committee at the University of Illinois in Chicago. The R6/2 and control mice used in this experiment were obtained by crossing wild type (WT) and ovary transplanted R6/2 mice expressing a polyglutamine tract of 160 ± 5 CAG repeats (B6CBA-R6/2, JAX #002810, The Jackson Laboratories, Bar Harbor, ME, USA) [10]. These animals were used for electron microscopy (Sect. 3.4). Littermates derived from this cross were further crossed with YFP(J16)$^{+/+}$ mice to produce YFP$^{+/-}$ (henceforth, YFP) and YFP$^{+/-}$ -R6/2 mice (henceforth YFP, R6/2 mice). These animals were used for MRI imaging and histology (Sects. 3.2 and 3.3). At the early symptomatic stage (P60), mice were anesthetized and transcardially perfused with PBS containing 4% paraformaldehyde (PFA). Brains were stored in PBS at 4 °C until MRI was performed. To evaluate brain morphology using fluorescence microscopy-based methods, we crossed homozygous YFP (J16) male mice (Thy-1, JAX #003709, The Jackson Laboratories, Bar Harbor, ME, USA) with R6/2 females. Brain tissue from YFP and YFP, R6/2 littermates was processed for fluorescence microscopic analysis as described in our prior work [10]. A total of 14 animals were used to complete all the experiments.

Magnetic resonance imaging

All scans were performed at the Advanced Magnetic Resonance Imaging and Spectroscopy (AMRIS) Facility (Gainesville, FL, USA) of the National High Magnetic Field Lab using a 750 MHz (17.6 T, 89-mm wide bore) Avance III HD imager-spectrometer (Bruker BioSpin, Billerica, MA, USA). Twenty-four hours before imaging, the fixed brains ($n = 6$ per experimental group) were washed in excess PBS and blindly assigned to two different groups. Each group of three brains (four MRI sessions) was stacked in a 20-mm diameter NMR tube using a custom-built 3D printed plastic holder to align three brains. The brains were then immersed in Fluorinert™ (3M™, FC-770) to establish a proton-free magnetic susceptibility matching environment. The NMR tube was tightly fit into a 20 mm diameter birdcage RF coil and inserted into the Micro-2.5 gradient set (1500 mT/m) of the spectrometer. The temperature of the samples reflected the cool bore temperature of the polarizing magnet (typically, 18–25 °C).

For acquiring data for the anomalous diffusion model, a stimulated echo diffusion-weighted pulse sequence was used with TR/TE values of 4000 ms/28 ms, four averages, and for the 2 cm diameter field of view, an in-plane resolution of 100 µm × 100 µm, and a slice thickness of 400 µm. The Stejskal–Tanner diffusion pulse sequence parameters used had a pulsewidth, δ, of 3.5 ms, a pulse separation, Δ, of 15.6 ms, and a gradient strength ranging from 183 to 1300 mT/m, corresponding to diffusion weighting b values of 400, 800, 1500, 3000, 5000, 7500, 10,000, 12,000, 15,000, and 20,000 s/mm^2. Three orthogonal diffusion gradient directions were acquired to generate a trace image for CTRW analysis. Total scan time was approximately 15 h.

DTI was also performed using a stimulated echo diffusion sequence, but with 200 µm isotropic resolution, two averages, and TR/TE values of 3000 ms/25 ms. For the DTI acquisition, we acquired two $b = 0$ measurements and used a Stejskal–Tanner pulse sequence applied in 12 gradient directions with a δ of 3.5 ms, a Δ of 15.6 ms, and a gradient strength of 356 mT/m, for a b value of 1500 s/mm^2. From these data, we calculated the eigenvalues and eigenvectors for the diffusion tensor. Following standard convention, the data are presented as the fractional anisotropy (FA), axial diffusivity (AD), radial diffusivity (RD), and mean diffusivity (MD) [15].

DTI data were analyzed using MRI Analysis Software (MAS), available from http://marecilab.mbi.ufl.edu. To calculate the CTRW parameters of Eq. (2), we wrote a dedicated MATLAB™ fitting routine that used the normalized trace data to fit α, β, and $D_{\alpha,\beta}$ by applying a Levenberg Marquadt minimization algorithm on a voxelwise basis. In this fitting, we used Padé approximations to the Mittag–Leffler function that was provided by C. Ingo and described in [18]. For the DTI and CTRW analyses, we centered our studies in six consecutive frontal coronal slices using four regions of interest (ROI) selected within the CC of WT and R6/2 symptomatic animals. In our previous work [18], we found that $\Delta = 17.3$ ms and $\delta = 3.5$ ms provided the best contrast in normal and fixed rat brain tissue; hence, here, we used very

similar parameters ($\Delta = 15.6$ ms and $\delta = 3.5$ ms) to study diffusion in the brains of mice with Huntington's disease—incrementing only the gradient strength to increase the b values. The parameter extraction algorithm for α, β, and $D_{\alpha,\beta}$ uses the stretched exponential function (which is the asymptotic low b value form of the Mittag–Leffler function) to select the initial values. The details of this decomposition are described in the Appendix to [18]. Using this method, the parameter fits for our data were reproducible and stable (see Suppl. Fig. 2), and consistent with the values reported in [18]. Additional information about approximating the Mittag–Leffler function is provided in the recent paper by C. Ingo and colleagues [36].

Quantitative fluorescence microscopy imaging and immunohistochemistry

After MRI, brains were placed in PBS with progressively increasing sucrose concentrations [5–30%] for an additional 24 h for cryo-protection. Following embedding in optical cutting temperature (OCT) polymer compound (Tissue-Tek, cat #4583 Sakura Finetek, Torrance, CA, USA), 50 µm-thick coronal brain sections were prepared using a Leica cryostat CM 1850. Sections were mounted on Superfrost slides (Fisher, Cat #12-550-15, Hampton, NH, USA), dried for 15 min and the OCT removed by washing three times with Tris-based saline buffer (TBS). YFP and YFP-R6/2 brain sections were mounted in Vecta-Shield mounting media (Vector Laboratories, Burlingame, CA, USA) and images acquired using a Leica LMS-710 confocal microscope. For immunostaining experiments, brain sections were permeabilized with TBS containing Triton-X100, 0.25% for 10 min, and then blocked with TBS containing 5% goat serum for an hour. Sections were incubated with TBS containing primary antibodies recognizing myelin basic protein (MBP; PhosphoSolution, Cat #1120-MBP 1:500 Aurora, CO, USA) or the astrocyte maker glial fibrillary acid protein (GFAP; NeuroMab Cat #75-240 1:50, Davis, CA, USA). Secondary anti-mouse IgG antibodies were from Invitrogen (Alexa Fluor 647 nm, Cat #A-21446 1:500, Thermo Fisher Scientific, Waltham, MA, USA). Quantitation of YFP and antibody-derived fluorescence was performed as described in our published work [10]. In parallel with the MRI data, we selected six consecutive axial brain slides, and we centered our analysis in four regions of interests in the corpus callosum.

Electron microscopy

Mice were anesthetized and intracardially perfused with Karnovsky fixative [37, 38] ($n = 1$ per experimental group). Brains were dissected, post-fixed in 1% OsO_4, dehydrated through a graded series of alcohols and propylene oxide, infiltrated, and embedded in araldite, as described in [39]. Ultrathin sections were prepared using a diamond knife (80–90 nm), collected in carbon-coated slot grids, and viewed in a JEOL 1220 TEM (JEOL USA, Peabody, MA, USA). Mouse brains were longitudinal sectioned, and one-half of the brain was used for the transverse and longitudinal sections of the CC. Four-to-five sections were obtained from each mouse and four images were acquired from each section. Additional analysis of axonal ultrastructure (axonal density) in the CC regions showed a significant increase in the HD mice group (see Suppl. Fig. 1).

Statistical analysis

The data were tabulated and analyzed using Graph Pad Prism 6 software (La Jolla, CA, USA). For quantitative analysis of diffusion coefficient values, un-paired Student t tests were used to determine statistical differences between experimental groups. Results were replicated by application of non-parametric statistical tools (Mann–Whitney test). A value of $p < 0.05$ was used to demonstrate statistical significance. Error bars in all the figures represent standard error of the mean (SEM).

Results

Comparative analysis of DTI and CTRW parameters to evaluate microstructural anomalies in the corpus callosum of R6/2 mice

Progressive degeneration of axon-rich white matter tracts in the corpus callosum (CC) represents a critical event in HD pathogenesis [40]. The mono-exponential MRI diffusion model (b values of 0 and 1500 s/mm^2) was used to fit the DTI data acquired from the brains of R6/2 mice. We calculated the AD, MD, RD, and FA for four consecutive coronal slices (stereotaxic coordinates from Praxinos, Bregma 1.32 mm) using matched regions of interest (ROI) selected within the CC of WT and R6/2 symptomatic animals (Fig. 1a). Consistent with the literature [41, 42], we found a 17% decrease in the FA for YFP, R6/2 brains (0.59 ± 0.05), compared with the FA of YFP brains (0.69 ± 0.04) ($p < 0.01$) in addition to an 11% increase in AD (YFP, R6/2 mice $= 6.8 \pm 0.06 \times 10^{-4}$ mm^2/s vs YFP mice $= 6.1 \pm 0.07 \times 10^{-4}$ mm^2/s) ($p < 0.01$), a 29% increase in RD (YFP, R6/2 mice $= 3.1 \pm 0.05 \times 10^{-4}$ mm^2/s vs YFP mice $= 2.2 \pm 0.04 \times 10^{-4}$ mm^2/s) ($p < 0.01$) as well as a 19% increase in MD (YFP, R6/2 mice $= 4.3 \pm 0.05 \times 10^{-4}$ mm^2/s vs YFP mice $= 3.5 \pm 0.05 \times 10^{-4}$ mm^2/s) ($p < 0.01$) (Fig. 1b).

The same data set described in Fig. 1 was fit to the CTRW model, and the derived fractional-order parameter maps are shown in (Fig. 2a). Overall, the $D_{\alpha,\beta}$, α, and β values

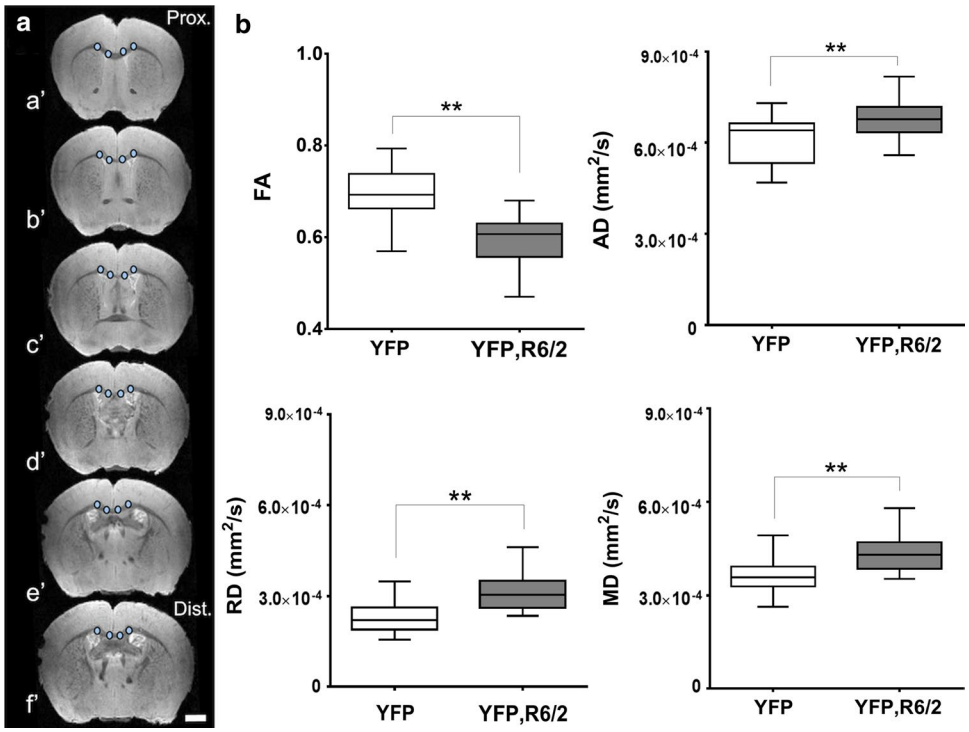

Fig. 1 Calculated diffusion tensor imaging (DTI) parameters from control and from Huntington's disease mouse brains. **a** Representative T2-weighted images ($b=0$) of coronal slices (a′–f′) from six consecutive frontal lobe regions of a mouse showing the four regions of interest (ROIs) centered in the corpus callosum (light blue circles) used in the DTI analysis. **b** Compiled data from Huntington's disease (YFP, R6/2) and control (YFP) mice box plots of the fractional anisotropy (FA), axial diffusivity (AD), radial diffusivity (RD), and mean diffusivity (MD), (**$p<0.01$), ($n=3$ mice per group). Scale bar = 1 mm

were lower in the Huntington's disease R6/2 mice than in the WT controls (Fig. 2b). For example, the fractional diffusion coefficient, $D_{\alpha,\beta}$, was reduced from 0.26×10^{-3} to 0.23 ± 10^{-3} mm^2/s ($p<0.05$). In addition, the α parameter was reduced by 21% (indicating more tissue heterogeneity [18]) from 0.39 ± 0.02 for the WT to 0.31 ± 0.01 for the R6/2 mice, a decrease that was significant at the $p<0.001$ level. In contrast, only a small decrease in the $\beta/2$ parameter was measured (from 0.82 in the WT mice to 0.80 in the R6/2 mice), a change that was not statistically significance. In the CTRW model, the β parameter corresponds to the tail of the jump distribution, which in this study appears to be unaffected by the disease process. The $2\alpha/\beta$ parameter, which is the exponent for the mean squared displacement in the CTRW model and is 1.0 for Gaussian diffusion and 0.5 for single file diffusion, was reduced by 14% from 0.49 in the WT to 0.42 in the R6/2 mice ($p<0.05$) (Fig. 2b).

Microscopic analysis reveals axonal pathology and cellular alterations in the corpus callosum of R6/2 mice

After MRI, the fixed brains were sliced and processed for quantitative fluorescence microscopy and for immunohistochemistry (IHC). The YFP-derived fluorescence analysis from selected ROIs in the corpus callosum (Fig. 3a) revealed a reorganization of the axons in the R6/2 mice characterized by a 26% decrease in overall YFP-derived fluorescence signal intensity (Fig. 3b) compared to the WT mice in arbitrary units (AU), YFP (R6/2), $9.4\pm0.5\times10^5$ AU vs YFP (WT) mice $=6.9\pm0.4\times10^5$ AU (***$p<0.001$) (Fig. 3c). This change appears from the slides to be associated with a reduction in axonal mass. The IHC analysis (Fig. 3b) showed a two–threefold increase in anti-glial fibrillary protein (GFAP) antibody immunoreactivity levels (R6/2 mice, $5.4\pm1.0\times10^4$ AU vs WT mice, $20.4\pm1.4\times10^4$ AU (Fig. 3c), (***$p<0.001$), a clear indication of astrogliosis at this stage of the disease. Similarly, the levels of anti-MBP immunoreactivity (Fig. 3b) were reduced by 71% in the R6/2 mice, ($5.4\pm0.3\times10^5$ AU vs WT mice $=1.5\pm0.3\times10^5$ AU (Fig. 3c), (***$p<0.001$), suggesting myelin and oligodendrocyte-related alterations. Additional calculations of axonal tortuosity (τ) in comparative CC regions used to calculate MRI parameters showed a significant increase of tortuosity index in the YFP, R6/2 mice group (see Suppl. Fig. 1).

Ultrastructural studies reveal structural changes and increased tortuosity of degenerating callosal axons in R6/2 mice corpus callosum

Ultrastructural examination using transmission electron microscopy (TEM) of longitudinal and axial axonal sections from the corpus callosum (CC) showed axonal degeneration. ImageJ-based analysis of the TEM images revealed a significant increase in axonal density, consistent with the marked reduction in CC volume detected by MRI in human HD patients [11]. Specifically, in transverse sections to the axons, we found a reduction in axonal

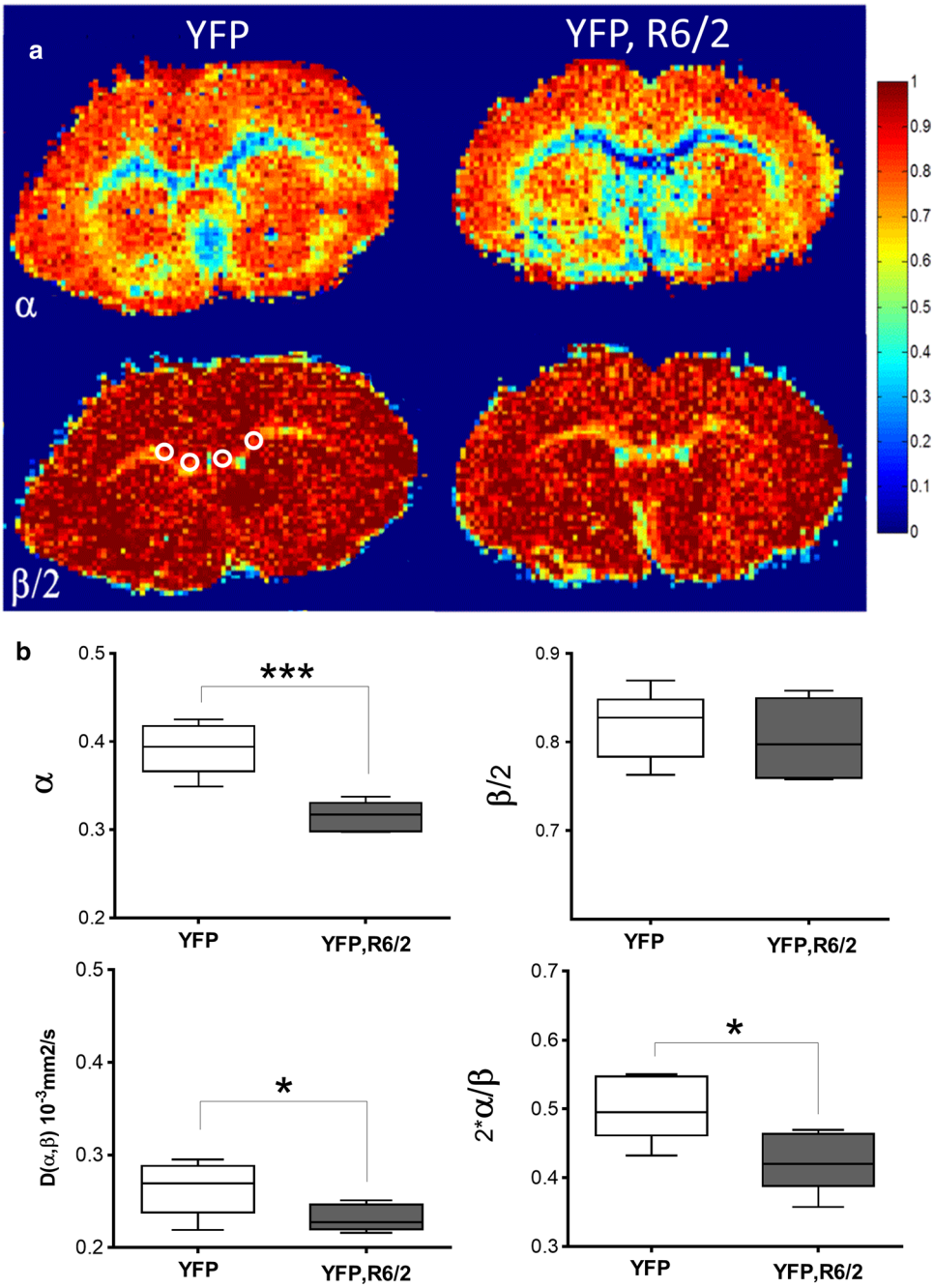

Fig. 2 Calculated anomalous diffusion parameters from control and from Huntington's disease mouse brains. **a** Coronal brain slices displaying anomalous diffusion brain maps for α and $\beta/2$ fractional order parameters from Huntington's disease (YFP, R6/2, right) and control (YFP, left) mice. Note the reduced α values in the corpus callosum (CC) of the YFP, R6/2 mice. **b** Statistical analysis of anomalous diffusion parameters based on selected CC ROIs (circles in $\beta/2$ map). Data showed significant differences in $D_{\alpha,\beta}$, α, and $2\alpha/\beta$ between the control and diseased animals ($^*p<0.05$). Note that the most significant differences between both groups were related to the parameter α ($^{***}p<0.001$) ($n=3$ mice per group). Scale bar = 1 mm

diameters (Fig. 4a) and myelin thickness and extra-axonal space (Fig. 4a′). In addition, there is an apparent increase in axonal packing density, and axonal tortuosity in corpus callosum axons from the R6/2 mice compared with WT controls (Fig. 4b). Thus, a quantitative analysis of axons located in the CC region used to calculate CTRW parameters showed a significant increase in axonal density in the HD mice group (see Suppl. Fig. 1).

Discussion

The goal of this work is to study the association of changes in WM integrity captured by DTI and CTRW parameters from a high field MRI (17.6 T) with cellular changes visualized by fluorescence and electron microscopy applied a well-established mouse model of HD (R6/2 mice). The

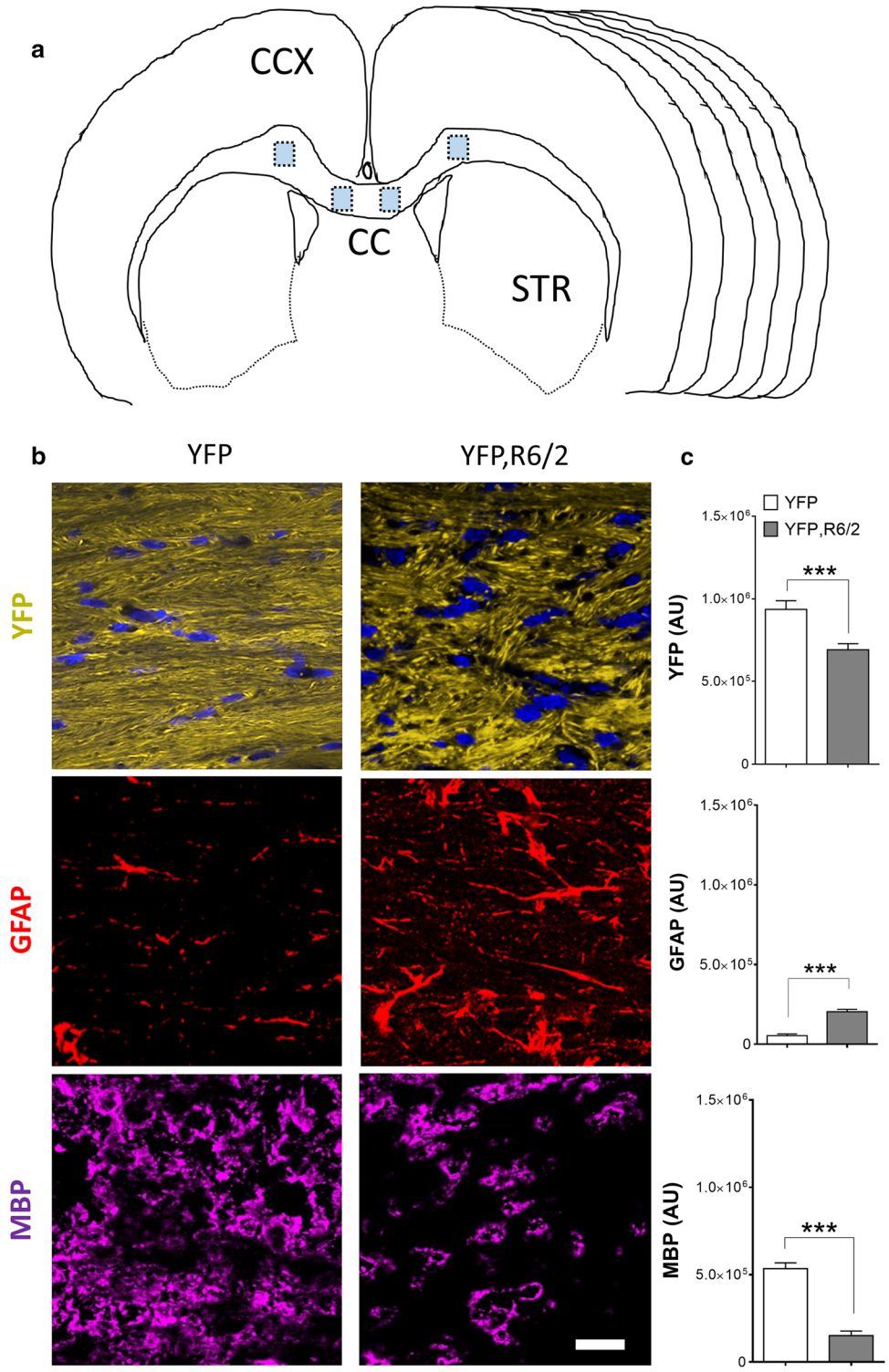

Fig. 3 Multi-cellular changes in the corpus callosum of the Huntington's disease mice reveals increased white matter complexity. **a** Diagram showing coronal sections and histological regions of interest (ROIs in light blue) centered in the corpus callosum (CC) between the cortex (CCX) and the striatum. **b** Coronal sections centered in the corpus callosum showing changes in neuronal architecture and axonal orientation by endogenous expression. Yellow fluorescent protein (YFP) can be observed in the R6/2 mice (YFP, R6/2). Note an increase of axonal tortuosity in the R6/2 mice. Nuclear counterstaining with DAPI (Blue). Astrocyte proliferation is labeled by glial fibrillary acid protein (GFAP) and can be observed in white matter (WM) in the HD mice. The amount of myelin basic protein (MBP)—a marker of oligodendrocyte function—is decreased in the HD mice. **c** Quantitative fluorescence analysis of white matter markers (YFP, GFAP, and MBP) in the corpus callosum of the R6/2 and WT mice (***$p < 0.001$) ($n = 6$ mice per group). *AU* Arbitrary Units. Scale bar = 10 µm

CTRW model is intermediate between a tissue compartmental analysis and a heuristic fit to the data. CTRW is a stochastic model, like kurtosis, which interpolates between the classical Gaussian description of diffusion and non-Gaussian propagator models used in characterizing anomalous diffusion [43]. The new idea in the CTRW model is to account for particle trapping, not by building models of the tissue microstructure, but by introducing a 'waiting' time into each step of the underlying Brownian motion, and to account for particle displacement by introducing a 'jump increment' after each rest [33]. Hence, the Brownian path trajectory is a balance of competing factors, one which

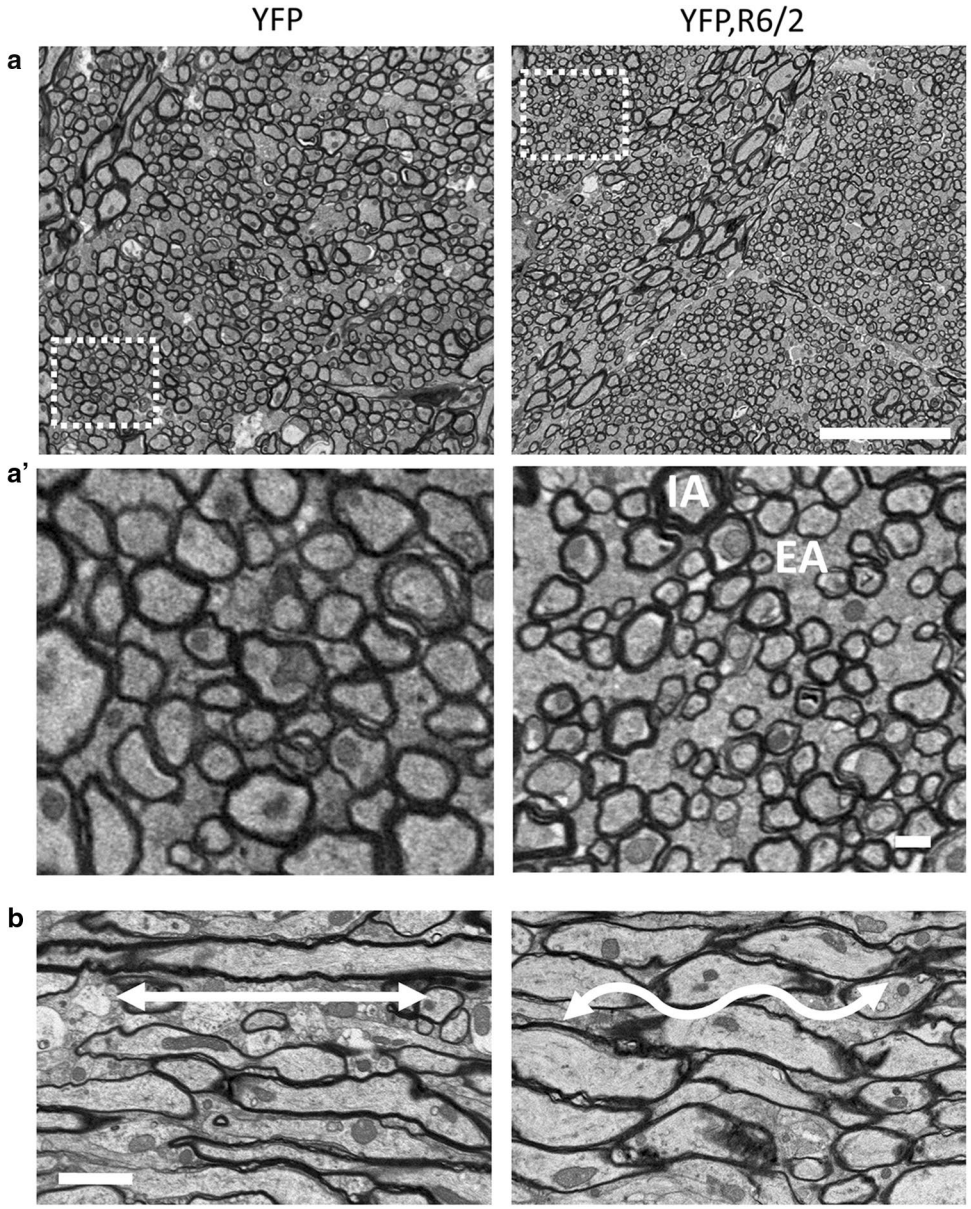

Fig. 4 Transmission electron microscopy shows complex ultrastructural axonal changes in the corpus callosum of the Huntington's disease mice R6/2. **a** Transmission electron microscopy (TEM) from white matter (cross sections) centered in the prefrontal region of the corpus callosum in the wild-type (WT) and Huntington's mice (R6/2) taken at ×6000 magnification. Scale bar = 10 µm. Note that axonal myelin sheets are stained in black by osmium tetroxide (OsO_4). **a′** Greater magnification from Fig. 4a (dotted white square) in WT and R6/2 mice shows a decrease in axonal diameters and a relative increase in extra-axonal space and axonal density in the R6/2 mice. Scale bar = 1 µm. **b** TEM from the corpus callosum WM (longitudinal section) showed an increase in axonal tortuosity (curved double-headed white arrow) compared to similar regions in the control mice (straight white double-headed arrow). *IA* intra-axonal compartment, *EA* extra-axonal compartment. Scale bar = 1 µm

describes sub-diffusion, compared with Gaussian motion, and the other, which describes super-diffusion [34]. Formally, the tendencies are introduced as separate inverse power laws for the waiting times and jump displacements, respectively [30]. Mathematically, the underlying statistical assumptions of the CTRW model generalize the order of the governing time and space derivatives into α and β, so that sharp fall offs in the likelihood of a long waiting time or a large particle displacement only occur when α and β are near the integer Gaussian case of $\alpha = 1$ and $\beta = 2$ (where the respective probabilities are Dirac delta functions) [32]. Physically, when $\alpha < 1$ and $\beta > 2$, the diffusion process can be viewed as a distribution of sub-compartments, each representing a fraction of particles that—compared with the case of Gaussian Brownian motion—are trapped or transiently tugged into a fast flowing eddy. For example, CTRW models are used in the earth sciences [44] to describe surface erosion due to wind and rain of a gully or canyon, with small grains of sand moving slowly down the slope via hindered and restricted diffusion, and small rocks not moving as all, until all of a sudden the nearby support wears away, and the stone rolls [44]. When applied to brain tissue, the CTRW is used to capture aspects of the tissue's structural complexity, indirectly via the association of $D_{\alpha,\beta}$ with hindered diffusion, α with trapped water (restricted diffusion), and β with perfusion and membrane permeability [18, 27].

MRI has proved to be a useful method for monitoring HD progression by measuring volume loss within the striatum [45]. As axonal pathology became increasingly recognized

as an early and critical pathogenic event in HD [46], methods that probe sub-voxel structure have been pursued. For example, changes in diffusion parameters such as the fractional anisotropy and the mean diffusivity have been reported in HD patients long before loss of cerebral mass occurs [47, 48]. The parallel organization of axons within the CC makes this major white matter brain structure particularly suitable as a site to detect axonal changes at presymptomatic disease stages [49]. DTI provides sub-voxel information from which one can map the fiber pathways, and fiber density and fiber track maps are used to distinguish changes in brain connectivity, as fibers are lost, rearranged, or rerouted [50, 52].

Current DTI models use the Gaussian, mono-exponential model for diffusion-weighed signal decay to express degeneration in WM microstructure in terms of changes in the mean diffusivity and fractional anisotropy [52]. In this study, we also fit the data—at high b values—to a CTRW model that has been shown to capture brain tissue complexity [18]. We also used fluorescence microscopy and IHC techniques, to confirm the microstructural imaging biomarkers suggested by the DTI and CTRW models. The application of these optical methods using a mouse model featuring mosaic YFP expression [53] confirmed a marked disorganization and partial loss of callosal axons, as well as astrogliosis and myelin deficits [54–56]. Extending these findings, TEM revealed increased geometrical complexity across degenerating axons in the R6/2 mice, a finding consistent with observations of CC degeneration in HD patients [58, 59].

Our results indicate that both the DTI and CTRW diffusion models provide evidence of microstructural alterations in the corpus callosum of the R6/2 mice (Figs. 1 and 2). Decreasing FA is correlated not only with increased clinical severity in HD [59], but also with alterations in WM brain microstructure [12] and demyelination [60]. In particular, the FA is able to distinguish cuprizone-induced demyelination from remyelination [61], while MD is sensitive to gliosis and relative density or packing of axonal bundles [35]. In this study, the DTI and CTRW analyses were confirmed by histochemical and ultrastructural data (Figs. 3 and 4). From the histological data (Fig. 3), astrocytes are significantly increased in the brain regions studied, which could increase cellularity, which in tumors is associated with an increase in the diffusion coefficient [20–22] and a decrease in the α value of the stretched exponential and the Mittag–Leffler function. Hence, it is not surprising that we observed similar changes in the MD and α in the afflicted animals. The CTRW parameters (particularly α) appear to correlate with changes in the TEM images (Fig. 4) that show a closer packing of axons and greater extracellular tortuosity in Huntington's disease—consistent with the published literature [21, 63]—and with the idea that waiting times increase (diffusion particle trapping) in step with greater tissue heterogeneity, as described in our previous studies [63].

Thus, the CTRW parameters provide information on the tortuosity of the tissue microenvironment [63, 64]. This result is similar to decreases in α found by others to be associated with increased tissue heterogeneity [64] and complexity [65]. However, the utility of the fractional β parameter as a biomarker of HD in our current experiments remains unclear, as changes in this parameter were not significant in this particular animal model or disease stage; a finding that will be pursued in the future in vivo experiments.

Conclusions

In this study, we present a histologically verified comparison of diffusion-weighted imaging (DTI) with the continuous time random walk (CTRW) model of anomalous diffusion in the case of developing pathology in the R6/2 mouse model of Huntington's disease. Changes in organization were detected in WM tracts using both DTI and the CTRW models, changes that histology showed correspond with axonal reorganization, myelin content reduction, and glial cell redistribution. The complex cellular changes in the WM during the development of HD were not completely described by the DTI model, and supplemental information was provided by the CTRW parameters. Specifically, the α parameter reduction appears to reflect the increased axonal density and tortuosity, while demyelination in the corpus callosum is in agreement with an increase in radial diffusivity and the observed decrease in the fractional anisotropy. The future directions for this work will focus on confirming the connection between the early stages of HD pathology and the observed changes in the CTRW parameters and on improving the sensitivity of the high b value diffusion-weighted MRI, so that in vivo studies of HD in animal models and clinical MRI scanners can be performed. Among the limitations to overcome before applying CTRW measures in vivo are the long acquisition time needed to collect data at multiple b values, and the need for high spatial resolution and a high signal-to-noise ratio.

Acknowledgements This work was support provided by grants from the National Center for Advancing Translational Science grant (NCATS TLTR000049 to AY), NIH DC02058 (to AL), CHDI (#A-11872; to GM and SB), NIH R21NS096642 (to GM). A portion of this work was performed in the McKnight Brain Institute at the National High Magnetic Field Laboratory's AMRIS Facility, which is supported by National Science Foundation Cooperative Agreement no. DMR-1157490 and the State of Florida. In addition, we would like to thank Mr. Dan Plant for his input and assistance in the design and experimental set up for this project, as well as Dr. Carson Ingo for his assistance in fitting the data to the Mittag–Leffler function.

Compliance with ethical standards

Conflict of interest Authors of this manuscript have no conflicts of interest to report.

Ethical approval Experiments were performed under protocols approved by the Animal Care Committee at the University of illinois in Chicago.

Statement on the welfare of animals All applicable international, national, and/or institutional guidelines for the care and use of animals were followed.

References

1. Harper PS (1992) The epidemiology of Huntington's disease. Hum Genet 89(4):365–376
2. Pringsheim T, Wiltshire K, Day L, Dykeman J, Steeves T, Jette N (2012) The incidence and prevalence of Huntington's disease: a systematic review and meta-analysis. Mov Disord 27(9):1083–1091
3. Walker FO (2007) Huntington's disease. Lancet 369(9557):218–228
4. Han I, You Y, Kordower JH, Brady ST, Morfini GA (2010) Differential vulnerability of neurons in Huntington's disease: the role of cell type-specific features. J Neurochem 113(5):1073–1091
5. Perez-Navarro E, Canals JM, Gines S, Alberch J (2006) Cellular and molecular mechanisms involved in the selective vulnerability of striatal projection neurons in Huntington's disease. Histol Histopathol 21(11):1217–1232
6. Pouladi MA, Morton AJ, Hayden MR (2013) Choosing an animal model for the study of Huntington's disease. Nat Rev Neurosci 14(10):708–721
7. Mangiarini L, Sathasivam K, Seller M, Cozens B, Harper A, Hetherington C, Lawton M, Trottier Y, Lehrach H, Davies SW, Bates GP (1996) Exon 1 of the HD gene with an expanded CAG repeat is sufficient to cause a progressive neurological phenotype in transgenic mice. Cell 87(3):493–506
8. Menalled L, El-Khodor BF, Patry M, Suarez-Farinas M, Orenstein SJ, Zahasky B, Leahy C, Wheeler V, Yang XW, MacDonald M, Morton AJ, Bates G, Leeds J, Park L, Howland D, Signer E, Tobin A, Brunner D (2009) Systematic behavioral evaluation of Huntington's disease transgenic and knock-in mouse models. Neurobiol Dis 35(3):319–336
9. Ramaswamy S, McBride JL, Kordower JH (2007) Animal models of Huntington's disease. ILAR J 48(4):356–373
10. Gatto RG, Chu Y, Ye AQ, Price SD, Tavassoli E, Buenaventura A, Brady ST, Magin RL, Kordower JH, Morfini GA (2015) Analysis of YFP(J16)-R6/2 reporter mice and postmortem brains reveals early pathology and increased vulnerability of callosal axons in Huntington's disease. Hum Mol Genet 24(18):5285–5298
11. Rosas HD, Lee SY, Bender AC, Zaleta AK, Vangel M, Yu P, Fischl B, Pappu V, Onorato C, Cha JH, Salat DH, Hersch SM (2010) Altered white matter microstructure in the corpus callosum in Huntington's disease: implications for cortical "disconnection". NeuroImage 49(4):2995–3004
12. Poudel GR, Stout JC, Dominguez DJ, Churchyard A, Chua P, Egan GF, Georgiou-Karistianis N (2015) Longitudinal change in white matter microstructure in Huntington's disease: the IMAGE-HD study. Neurobiol Dis 74:406–412
13. Poudel GR, Stout JC, Dominguez DJ, Salmon L, Churchyard A, Chua P, Georgiou-Karistianis N, Egan GF (2014) White matter connectivity reflects clinical and cognitive status in Huntington's disease. Neurobiol Dis 65:180–187
14. Rosas HD, Tuch DS, Hevelone ND, Zaleta AK, Vangel M, Hersch SM, Salat DH (2006) Diffusion tensor imaging in presymptomatic and early Huntington's disease: selective white matter pathology and its relationship to clinical measures. Mov Disord 21(9):1317–1325
15. Le Bihan D (2013) Apparent diffusion coefficient and beyond: what diffusion MR imaging can tell us about tissue structure. Radiology 268(2):318–322
16. Tabesh A, Jensen JH, Ardekani BA, Helpern JA (2011) Estimation of tensors and tensor-derived measures in diffusional kurtosis imaging. Magn Reson Med 65(3):823–836
17. Zhang H, Schneider T, Wheeler-Kingshott CA, Alexander DC (2012) NODDI: practical in vivo neurite orientation dispersion and density imaging of the human brain. NeuroImage 61(4):1000–1016
18. Ingo C, Magin RL, Colon-Perez L, Triplett W, Mareci TH (2014) On random walks and entropy in diffusion-weighted magnetic resonance imaging studies of neural tissue. Magn Reson Med 71(2):617–627
19. Yu Q, Reutens D, O'Brien K, Vegh V (2016) Tissue microstructure features derived from anomalous diffusion measurements in magnetic resonance imaging. Hum Brain Mapp 38(2):1068–1081
20. Karaman MM, Sui Y, Wang H, Magin RL, Li Y, Zhou XJ (2016) Differentiating low- and high-grade pediatric brain tumors using a continuous-time random-walk diffusion model at high b-values. Magn Reson Med 76(4):1149–1157
21. Xu B, Su L, Wang Z, Fan Y, Gong G, Zhu W, Gao P, Gao JH (2017) Anomalous diffusion in cerebral glioma assessed using a fractional motion model. Magn Reson Med 78(5):1944–1949
22. Karaman MM, Wang H, Sui Y, Engelhard HH, Li Y, Zhou XJ (2016) A fractional motion diffusion model for grading pediatric brain tumors. NeuroImage Clinical 12:707–714
23. Gatto RG, Li W, Magin RL (2018) Diffusion tensor imaging identifies presymptomatic axonal degeneration in the spinal cord of ALS mice. Brain Res 1679:7
24. Alexander AL, Lee JE, Lazar M, Field AS (2007) Diffusion tensor imaging of the brain. Neurotherapeutics 4(3):316–329
25. Gatto RG (2018) Diffusion tensor imaging as a tool to detect presymptomatic axonal degeneration in a preclinical spinal cord model of amyotrophic lateral sclerosis. Neural Regen Res 13(3):425–426
26. Metzler R, Klafter J (2000) The random walk's guide to anomalous diffusion: a fractional dynamics approach. Phys Rep 339:1–77
27. Magin RL, Ingo C, Colon-Perez L, Triplett W, Mareci TH (2013) Characterization of anomalous diffusion in porous biological tissues using fractional order derivatives and entropy. Microporous Mesoporous Mater 178:39–43
28. Klages R, Radons G, Sokolov IM (eds) (2012) Anomalous transport: foundations and applications. Wiley, Weinheim
29. Magin RL, Abdullah O, Baleanu D, Zhou XJ (2008) Anomalous diffusion expressed through fractional order differential operators in the Bloch–Torrey equation. J Magnetic Resonance 190(2):255–270
30. Gorenflo RMF, Moretti D, Pagnini G, Paradisi P (2002) Fractional diffusion: probability distributions and random walk models. Phys A 305(1–2):106–112
31. Wen CSH, Zhanga X, Korosak D (2010) Anomalous diffusion modeling by fractal and fractional derivatives. Comput Math Appl 59(5):1754–1758
32. Lenzi EK, Ribeiro HV, Tateishi AA, Zola RS, Evangelista LR (2016) Anomalous diffusion and transport in heterogeneous systems separated by a membrane. Proc Math Phys Eng Sci 472(2195):20160502

33. Klafter J, Lim SC, Metzler R (eds) (2011) Fractional dynamics: recent advances. World Scientific, Sinapore
34. Mainardi F (2000) Fractional calculus and waves in linear viscoelasticity: an introduction to mathematical models. Imperial College Press, London
35. Ingo C, Magin RL, Parrish TB (2014) New insights into the fractional order diffusion equation using entropy and kurtosis. Entropy 16(11):5838–5852
36. Ingo C, Barrick TR, Webb AG, Ronen I (2017) Accurate Padé global approximations for the Mittag–Leffler function, its inverse, and its partial derivatives to efficiently compute convergent power series. Int J Appl Comput Mat 3:347–362
37. Mount SL, Schwarz JE, Taatjes DJ (1997) Prolonged storage of fixative for electron microscopy: effects on tissue preservation for diagnostic specimens. Ultrastruct Pathol 21(2):195–200
38. Karnovsky MJ (1965) A formaldehyde-glutaraldehyde fixative of high osmolality for use in electron microscopy. J Cell Biol 27:137A–138A
39. Vranceanu F, Perkins GA, Terada M, Chidavaenzi RL, Ellisman MH, Lysakowski A (2012) Striated organelle, a cytoskeletal structure positioned to modulate hair-cell transduction. Proc Natl Acad Sci USA 109(12):4473–4478
40. Shaffer JJ, Ghayoor A, Long JD, Kim RE, Lourens S, O'Donnell LJ, Westin CF, Rathi Y, Magnotta V, Paulsen JS, Johnson HJ (2017) Longitudinal diffusion changes in prodromal and early HD: evidence of white-matter tract deterioration. Hum Brain Mapp 38(3):1460–1477
41. Phillips O, Squitieri F, Sanchez-Castaneda C, Elifani F, Caltagirone C, Sabatini U, Di Paola M (2014) Deep white matter in Huntington's disease. PLoS One 9(10):e109676
42. Phillips OR, Joshi SH, Squitieri F, Sanchez-Castaneda C, Narr K, Shattuck DW, Caltagirone C, Sabatini U, DiPaola M (2016) Major superficial white matter abnormalities in Huntington's disease. Front Neurosci 10:197
43. Symms M, Jager HR, Schmierer K, Yousry TA (2004) A review of structural magnetic resonance neuroimaging. J Neurol Neurosurg Psychiat 75(9):1235–1244
44. Höfling F, Franosch T (2013) Anomalous transport in the crowded world of biological cells. Rep Prog Phys 76:046602
45. Schumer R, Meerschaert MM, Baeumer B (2009) Fractional advection–dispersion equations for modeling transport at the Earth surface. J Geophys Res 114:F00A07
46. Morton AJ, Glynn D, Leavens W, Zheng Z, Faull RL, Skepper JN, Wight JM (2009) Paradoxical delay in the onset of disease caused by super-long CAG repeat expansions in R6/2 mice. Neurobiol Dis 33(3):331–341
47. Li H, Li SH, Yu ZX, Shelbourne P, Li XJ (2001) Huntingtin aggregate-associated axonal degeneration is an early pathological event in Huntington's disease mice. J Neurosci 21(21):8473–8481
48. Liu W, Yang J, Burgunder J, Cheng B, Shang H (2016) Diffusion imaging studies of Huntington's disease: a meta-analysis. Park Relat Disord 32:94–101
49. Matsui JT, Vaidya JG, Johnson HJ, Magnotta VA, Long JD, Mills JA, Lowe MJ, Sakaie KE, Rao SM, Smith MM, Paulsen JS (2014) Diffusion weighted imaging of prefrontal cortex in prodromal Huntington's disease. Hum Brain Mapp 35(4):1562–1573
51. Van Camp N, Blockx I, Camon L, de Vera N, Verhoye M, Veraart J, Van Hecke W, Martinez E, Soria G, Sijbers J, Planas AM, Van der Linden A (2012) A complementary diffusion tensor imaging (DTI)-histological study in a model of Huntington's disease. Neurobiol Aging 33(5):945–959
51. Phillips O, Sanchez-Castaneda C, Elifani F, Maglione V, Di Pardo A, Caltagirone C, Squitieri F, Sabatini U, Di Paola M (2013) Tractography of the corpus callosum in Huntington's disease. PLoS One 8(9):e73280
52. Mori S, Crain BJ, Chacko VP, van Zijl PC (1999) Three-dimensional tracking of axonal projections in the brain by magnetic resonance imaging. Ann Neurol 45(2):265–269
53. Weaver KE, Richards TL, Liang O, Laurino MY, Samii A, Aylward EH (2009) Longitudinal diffusion tensor imaging in Huntington's Disease. Exp Neurol 216(2):525–529
54. Porrero C, Rubio-Garrido P, Avendano C, Clasca F (2010) Mapping of fluorescent protein-expressing neurons and axon pathways in adult and developing Thy1-eYFP-H transgenic mice. Brain Res 1345:59–72
55. Chan CS, Surmeier DJ (2014) Astrocytes go awry in Huntington's disease. Nat Neurosci 17(5):641–642
56. Huang B, Wei W, Wang G, Gaertig MA, Feng Y, Wang W, Li XJ, Li S (2015) Mutant huntingtin downregulates myelin regulatory factor-mediated myelin gene expression and affects mature oligodendrocytes. Neuron 85(6):1212–1226
57. Bartzokis G, Lu PH, Tishler TA, Fong SM, Oluwadara B, Finn JP, Huang D, Bordelon Y, Mintz J, Perlman S (2007) Myelin breakdown and iron changes in Huntington's disease: pathogenesis and treatment implications. Neurochem Res 32(10):1655–1664
58. Crawford HE, Hobbs NZ, Keogh R, Langbehn DR, Frost C, Johnson H, Landwehrmeyer B, Reilmann R, Craufurd D, Stout JC, Durr A, Leavitt BR, Roos RA, Tabrizi SJ, Scahill RI (2013) Corpus callosal atrophy in premanifest and early Huntington's disease. J Huntingt Dis 2(4):517–526
59. Gomez-Tortosa E, MacDonald ME, Friend JC, Taylor SA, Weiler LJ, Cupples LA, Srinidhi J, Gusella JF, Bird ED, Vonsattel JP, Myers RH (2001) Quantitative neuropathological changes in presymptomatic Huntington's disease. Ann Neurol 49(1):29–34
60. Chilla GS, Tan CH, Xu C, Poh CL (2015) Diffusion weighted magnetic resonance imaging and its recent trend-a survey. Quant Imag Med Surg 5(3):407–422
61. Zhang J, Jones MV, McMahon MT, Mori S, Calabresi PA (2012) In vivo and ex vivo diffusion tensor imaging of cuprizone-induced demyelination in the mouse corpus callosum. Magn Reson Med 67:750–759
62. Ryutaro Y, Junichi H, Yoshifumi A, Fumiko S, Keitaro Y, Yuji K, Hideyuki O, Kenji FT (2018) Quantitative temporal changes in DTI values coupled with histological properties in cuprizone-induced demyelination and remyelination. Neurochem Intern 119:151–158
63. Liang Y, Ye AQ, Chen W, Gatto RG, Colon-Perez L, Mareci TH, Magin RL (2016) A fractal derivative model for the characterization of anomalous diffusion in magnetic resonance imaging. Commun Nonlinear Sci Numer Simul 39:529–537
64. Ingo C, Sui Y, Chen Y, Parrish TB, Webb AG, Ronen I (2015) Parsimonious continuous time random walk models and kurtosis for diffusion in magnetic resonance of biological tissue. Front Phys 3:11
65. Hrabe J, Hrabetova S, Segeth K (2004) A model of effective diffusion and tortuosity in the extracellular space of the brain. Biophys J 87(3):1606–1617
66. Sui Y, Wang H, Liu G, Damen FW, Wanamaker C, Li Y, Zhou XJ (2015) Differentiation of low- and high-grade pediatric brain tumors with high b-value diffusion-weighted MR imaging and a fractional order calculus model. Radiology 277(2):489–496